

A robust and tunable Luttinger liquid in correlated edge of transition-metal second-order topological insulator $\text{Ta}_2\text{Pd}_3\text{Te}_5$

Received: 11 October 2022

Accepted: 2 November 2023

Published online: 23 November 2023

 Check for updates

Anqi Wang^{1,2,6}, Yupeng Li^{1,6}, Guang Yang^{1,6}, Dayu Yan^{1,6}, Yuan Huang^{1,3}, Zhaopeng Guo¹, Jiacheng Gao^{1,2}, Jierui Huang^{1,2}, Qiaochu Zeng¹, Degui Qian¹, Hao Wang¹, Xingchen Guo^{1,2}, Fanqi Meng¹, Qinghua Zhang^{1,4}, Lin Gu^{1,2,5}, Xingjiang Zhou^{1,2,5}, Guangtong Liu^{1,5}, Fanming Qu^{1,2,5}, Tian Qian^{1,5}, Youguo Shi^{1,2,5} ✉, Zhijun Wang^{1,2} ✉, Li Lu^{1,2,5} ✉ & Jie Shen^{1,5} ✉

The interplay between topology and interaction always plays an important role in condensed matter physics and induces many exotic quantum phases, while rare transition metal layered material (TMLM) has been proved to possess both. Here we report a TMLM $\text{Ta}_2\text{Pd}_3\text{Te}_5$ has the two-dimensional second-order topology (also a quadrupole topological insulator) with correlated edge states - Luttinger liquid. It is ascribed to the unconventional nature of the mismatch between charge- and atomic- centers induced by a remarkable double-band inversion. This one-dimensional protected edge state preserves the Luttinger liquid behavior with robustness and universality in scale from micro- to macro- size, leading to a significant anisotropic electrical transport through two-dimensional sides of bulk materials. Moreover, the bulk gap can be modulated by the thickness, resulting in an extensive-range phase diagram for Luttinger liquid. These provide an attractive model to study the interaction and quantum phases in correlated topological systems.

Whereas topological systems without consideration of correlation have been studied widely in the last decades, the exotic quantum phases derived from the interaction between electrons and topological state have recently attracted great attention¹, such as quantum spin liquids² and topological Mott insulators³ which possess one-dimensional (1D) bosonic mode with spin-charge separation, strongly correlated Chern insulators in flat bands of magic-angle twisted bilayer graphene^{4,5} and topological superconductors for topological quantum computation^{6,7}. The aforementioned correlated 1D bosonic mode is described as Tomonoga–Luttinger liquid (simplified as Luttinger liquid, LL), and characterized by a power-law vanishing to anomaly zero density-of-state at the Fermi level. This power-law behavior in electrical transport

measurements has been harnessed to experimentally test LL in the edge states of quantum spin Hall insulator candidates^{8–10} and quantum Hall systems^{11–16}. Thus, LL quantum phase provides a powerful tool to analyze the correlated 1D edge state emerging from topological order. However, in these systems, the LL relies on the microscopic details and is lack of experimental evidence for its universality and robustness, let alone extending to macro-scale, which is supposed to be a signature for topological order. Moreover, this vulnerability leads to the absence of the quantitative test of LL, e.g., its exponent factor as the Coulomb interaction strength, in the edge state of topological system, though a large amount of theories have discussed the possibility of taking into account different interactions^{17–21}.

¹Beijing National Laboratory for Condensed Matter Physics, Institute of Physics, Chinese Academy of Sciences, Beijing 100190, China. ²School of Physical Sciences, University of Chinese Academy of Sciences, 100049 Beijing, China. ³Advanced Research Institute of Multidisciplinary Science, Beijing Institute of Technology, 100081 Beijing, China. ⁴Yangtze River Delta Physics Research Center Co. Ltd, 213300 Liyang, China. ⁵Songshan Lake Materials Laboratory, 523808 Dongguan, China. ⁶These authors contributed equally: Anqi Wang, Yupeng Li, Guang Yang, Dayu Yan. ✉e-mail: ygshi@iphy.ac.cn; wzj@iphy.ac.cn; lilu@iphy.ac.cn; shenjie@iphy.ac.cn

On the other hand, unlike a two-dimensional (2D) topological insulator with gapless edge states, a 2D second-order topological insulator (SOTI, or a quadrupole topological insulator) is supposed to have gapped edge states and in-gap corner states (in the presence of chiral symmetry)²². Although many 2D SOTI candidates have been proposed in literature^{23–27}, rare transition-metal compound has been predicted to be a 2D SOTI. After considering many-body interactions, superconductivity, excitonic condensation and Luttinger liquid can be expected in bulk and edge states of the transition-metal SOTI.

Here, we have observed the LL inhabiting the edge states, which are as the remnants of the 2D second-order topology, of a TMLM Ta₂Pd₃Te₅. Through the first-principles calculations, we demonstrate that this topological state originates from a remarkable double-band inversion and results in an unconventional nature with an essential band representation $A''@4c^{28}$. Then we have performed the electrical transport measurements of tens of Ta₂Pd₃Te₅ bulk and thin-film devices, and detected the coexistence of the bulk insulating gap, the in-gap edge conducting state and the edge gap as the signature of the 2D SOTI. Interestingly, the edge state displays a universal scaling of power-law relation with a zero-energy anomaly as a function of temperature (T) and energy (signed as the voltage bias here), which is considered as the critical evidence of LL. The weak van der Waals (vdW) interaction between layers allows this LL to be reproducible in the edge channels of all the devices from atomic- to macro-scale, with a conductance proportional to the edge geometry. That is the 2D side facets of macroscopic bulk also show 1D LL anisotropic electrical transport. This reveals for the first time the evidence of a scale connection from atomic- to macro-LL, and supports this LL quantum state with universality and robustness irrespective of the microscopic details. In addition, the coexistence of the three states induces a tunability of the LL power-law exponent to represent the strength of Coulomb interaction, as well as a reversible LL-Fermi liquid (FL) transition and a full phase diagram. All these demonstrate a robust and universal LL with the many precise-controlled parameters, as an

effective tool to characterize the interaction and the quantum phase transition in the correlated topological system.

Crystal structure

Ta₂Pd₃Te₅ is a vdW material with quasi-one-dimensional (Q1D) Ta₂Te₅ chains and crystallizes in needle-like single crystals along the b -direction (see the crystal structure and the optical image of the typical samples in Fig. 1a and ref. 29). The single crystal is synthesized with an orthorhombic structure $Pnma$ (space group No.62)²⁹. The Q1D characteristic and layered structure are confirmed by high-resolution scanning transmission electron microscope (STEM) images of Ta₂Pd₃Te₅ single crystal along [010] and [001] projections, revealing a thickness of ~ 0.7 nm for monolayer (Fig. 1b and Supplementary Fig. 1b, c). Because of the strong anisotropic bonding energy²⁹, this material is easy to mechanically exfoliate into large and thin films with flat and uniform edges along the Q1D chain (Supplementary Fig. 1a). Importantly, the Fermi level naturally locates in the bottom of conduction bands (Fig. 1c and Supplementary Fig. 1d), enabling a high-efficient modulation by the electrostatic gate. The coupling between vdW layers is weak, proved by the angle resolved photoemission spectroscopy (APRES) measurement (Fig. 1d and Supplementary Fig. 1e, f).

Theoretical calculation

Recently, the Perdew–Burke–Ernzerhof (PBE) calculations with spin-orbit coupling (SOC) predict that its monolayer is a quantum spin Hall state with a tiny SOC gap and the bulk topological crystalline insulator without a global band gap (ref. 29). However, both of the scanning tunneling microscopy (STM) (ref. 30) and APRES (Fig. 1c) measurements detect a bulk gap of ~ 50 meV. As reported in ref. 29, the nearly zero-energy band gap is sensitive to the lattice constant. On the other hand, the experimental energy gap can be induced by many-body interactions in the Q1D structure, like electron-phonon interaction or electron-hole attractive interaction, as the excitonic state is thermodynamically most stable in a zero-gap semiconductor. Although the

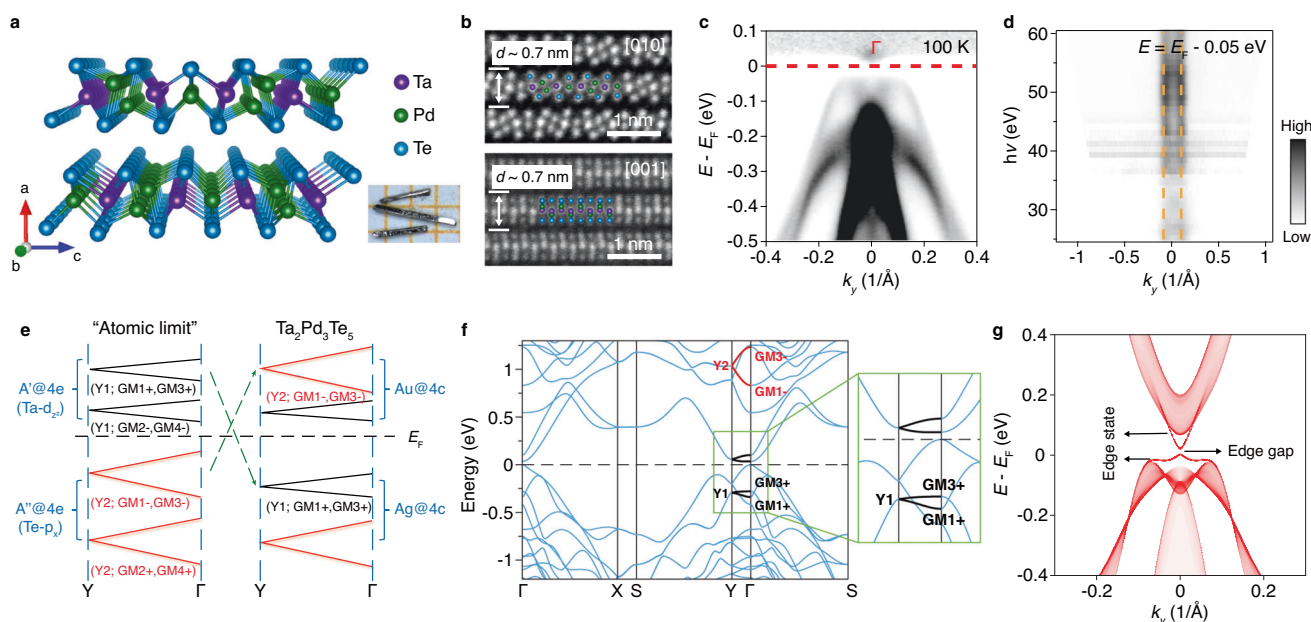


Fig. 1 | Crystal structure and band structure for Ta₂Pd₃Te₅. **a** Crystal structure viewed from the chain direction along the b -axis. Inset: Optical image of single crystals. Side length of the square is 1 mm. **b** Cross-sectional STEM images of Ta₂Pd₃Te₅ single crystal along [010] (up) and [001] (down) direction. **c** ARPES intensity plot of the band structure along the Γ - Y direction at $T = 100$ K. For clarity, the data is divided by the Fermi-Dirac distribution function to visualize the conduction band bottom above E_F . **d** Intensity plot of ARPES data at $E = E_F - 0.05$ eV

(valence band maximum) collected in a range of photon energies from 25 to 60 eV which shows weak coupling between Ta₂Pd₃Te₅ vdW layers. **e** The diagram of double-band inversion along Y - Γ line (adapted from ref. 28). **f** The modified band structure by adding 0.1 eV onsite energy on Ta- d_{z^2} states to simulate the gapped band structure with interactions. **g** The 1D gapped edge state of the 2D quadrupole topological insulator. The onsite energy is slightly modified in order to match the experimental energy gap.

exact reason of the bulk gap opening needs further investigations, the double-band inversion happens clearly between the $\{Y2;GM1-,GM3-\}$ and $\{Y1;GM1+,GM3+\}$ bands, which are 0.3 eV (or higher) away from the Fermi level in the monolayer structure of SG59 (imposing inversion; Supplementary Tables 1 and 2)²⁸. The schematic of the double band inversion in the system is given in Fig. 1e. Hence, in this manuscript, we focus on the modified band structure of the monolayer $Ta_2Pd_3Te_5$ (by adding small onsite energy to simulate the many-body gap opening) in Fig. 1f³¹. The band representation (BR) decomposition of the occupied bands shows that there is an essential BR at vacancies, suggesting the unconventional nature/obstructed atomic limit with second-order topology^{31,32}. A 2D quadrupole topological insulator with second-order topology possesses 1D gapped edge states and isolated corner states (Detailed information can be found in ref. 28). In the computed (01)-edge spectrum of Fig. 1g, the gapped edge states are clearly shown in the gap of the bulk continuum. The observed in-gap edge states as the remnants of the quadrupole topological insulator can exhibit 1D feature well, which is responsible for the observed LL behavior (will be analyzed later). In addition, since the layers of the bulk are vdW coupled (Fig. 1d and Supplementary Fig. 1e, f), the 1D edge states can still survive on the side surfaces of the bulk.

Three features in dI/dV curves

To investigate the electronic properties, we show the typical result for thin-film devices #A1,2 with thickness ~10 nm in Fig. 2, with a back-gate voltage V_{bg} tuning the chemical potential as illustrated in Fig. 2a. Figure 2b, c show the four-terminal measurement configurations and gate tunable dI/dV for devices #A1,2. Once applying the voltage bias (V_{DC}), the differential conductance ($dI/dV(V_{DC})$) curve of #A1 at charge neutral point (CNP, $V_{bg} = -28V$) shows distinguishable three regions (Fig. 2d, indicated by the purple–green–orange background). The first region at small V_{DC} indicates a gap structure (highlighted by the purple background, also see the conductance valley plotted by the symmetric V_{DC} in the inset of Fig. 2d), which closes around $T = 3.75 K$; The second region at medium V_{DC} reveals a power-law shape with an exponent of -0.33 (highlighted by the green background); The third region at high V_{DC} shows a new shape of enhanced conductance with increasing V_{DC} . Those regions are also repeated in other devices (Fig. 2e for device #A2 and Supplementary Fig. 12l, m). Notably, for device #A2, the T -dependent $dI/dV(T)$ curve at CNP (purple curve in Fig. 2f) shows similar three regions, which are semiconductor behavior with an energy gap of $-27 meV$ from 300 to $-50 K$, a power-law dependence with the exponential factor α of -0.79 from $-30 K$ to $6 K$ and another semiconductor behavior with a smaller energy gap of $-0.6 meV$ at lower T . This is clearer in the $\log(dI/dV)$ v.s. $1/T$ plot in the inset where the yellow dot dash lines are fitting curves of Arrhenius equation $dI/dV(T) \propto \exp(-\Delta/2k_B T)$. Similar behavior is repeatable, e.g., device #A4 with a $\sim 33 meV$ gap at high T and a $\sim 0.9 meV$ gap at low T in Supplementary Fig. 2. Apparently, this three-region feature fits the theoretical result of band structure with the bulk gap E_b , edge conducting state and edge gap E_e very well.

It should be noted that these devices are measured with four-terminal configuration with standard lock-in measurement and the phases θ of the lock-in amplifier are also small enough. So, the very-low- T behaviors do not come from the contact resistance which is not included in the measurement. In addition, the gap size we extracted from the Arrhenius equation is consistent with the thermal excitation energy of the temperature at which the gap behavior appeared. We also measured $dI/dV(V_{DC})$ and $dI/dV(T)$ from CNP to positive back-gate voltage (V_{bg}) (Fig. 2e, f). As the Fermi level moves up via applying positive V_{bg} sketched in Fig. 2a, the three-region feature gradually transitions into that of two regions without E_e in both $dI/dV(V_{DC})$ and $dI/dV(T)$ curves, further consistent with the calculated band structure.

Validation of edge state

To better clarify where the three structures respectively come from, we perform the nonlocal transport measurement based on Hall bar configuration³³. For a classical planar Hall bar, when a local voltage V_0 is applied, the nonlocal response V_{nl} at remote contacts will decay exponentially with distance, irrespective of T , chemical potential μ and so on. Whereas, the nonlocal voltages through edge channels don't rely on the distance³⁴. Figure 3a is a typical example of device #A3 with local and nonlocal measurement configuration (see Supplementary Fig. 5 for nonlocal measurement of device #A2). For the nonlocal conductance in Fig. 3c, d, both of nonlocal ratios V_{nl1}/V_0 and V_{nl2}/V_0 at CNP increase with decreasing T gradually between 50 and 120 K (see the orange region in insets of Fig. 3c, d), which are due to the reduced contact resistance of local electrodes and still behave as the classical ohmic planar fluid (the dash lines in the inset are classical planar values obtained by the simulation in Supplementary Fig. 6). Afterwards, they grow drastically on cooling from 50 K to 9 K (the green region), reaching values far above the classical values and indicating the edge transport case. Particularly, the sum of these two nonlocal ratios is close to 1 around 6 K. In the same T region (Fig. 3b), a power-law region appears in the local conductance fitted by the dash line (inset) and revealing it is the edge state. Interestingly below 4 K when the local conductance enters the E_e (purple region), V_{nl1}/V_0 comes up to 1 and V_{nl2}/V_0 goes to zero, suggesting that the inhomogeneity in E_e between different edge channels is enhanced. $V_{nl1}/V_0(V_{bg})$ curves at low T in Fig. 3c, d show nonlocal values become classic ohmic planar-like when Fermi level goes towards the conduction band at positive V_{bg} , excluding these unusual nonlocal values are due to planar fluid with extreme-disordered cases, e.g., with cracks or being broken into pieces. Therefore, by comparing the local and nonlocal measurements at different T and V_{bg} , we deduce both of the power-law feature and the small gap E_e root in the edge channels. This also excludes E_e from any bulk insulating state, e.g., Mott insulator or Anderson insulator, in particular with the phenomena of the greatly tunable T range at samples with varying thickness (will be analyzed more later in section 'Luttinger liquid phase diagram').

More evidence to prove this edge state is that while both APRES (Fig. 1c) and STM (ref. 30) clearly detect a large gap up to $\sim 50 meV$ on the top surface of $Ta_2Pd_3Te_5$ single crystal, the transport measurements still show large conductance around CNP on thin films exfoliated from the same bulk sample. Some of the conductance even reach a value as high as $2G_0$ (G_0 is the quantized conductance $2e^2/h$). STM measurement also reveals a distinct local conducting edge state in the bulk energy gap³⁰. Additionally, the similar edge conductivity in power-law region for samples with various thickness further confirms the existence of robust edge states from atomic- to macroscopic- scale and will be analyzed in detail in section 'Robust and universal Luttinger liquid from micro- to macro- size'. Moreover, the finite conductance around CNP, compared with the close-to-zero conductance when grounding the edge, also supports the existence of edge states (Supplementary Fig. 7). In conclusion, all the local and nonlocal measurements prove the existence of bulk state, edge conducting state and correlated edge gap, namely the second-order topology in this material.

Tunable Luttinger liquid in edge states

Now let's discuss the power-law relation of the edge state. Such behavior in 1D quantum system is a typical signature of LL, in particular with a universal scaling. We use device #A4 as a typical example whose behavior is similar to device #A2. Figure 4a shows in $dI/dV(V_{DC})$ curves for device #A4 at $V_{bg} = 0V$, E_e disappears and power-law relation dominates at higher T (other systematic data of device #A4 are shown in Supplementary Fig. 2). For those $dI/dV(V_{DC})$ curves without E_e behavior (from $T = 12.9 K$ to $39.8 K$), in Fig. 4b we scaled the

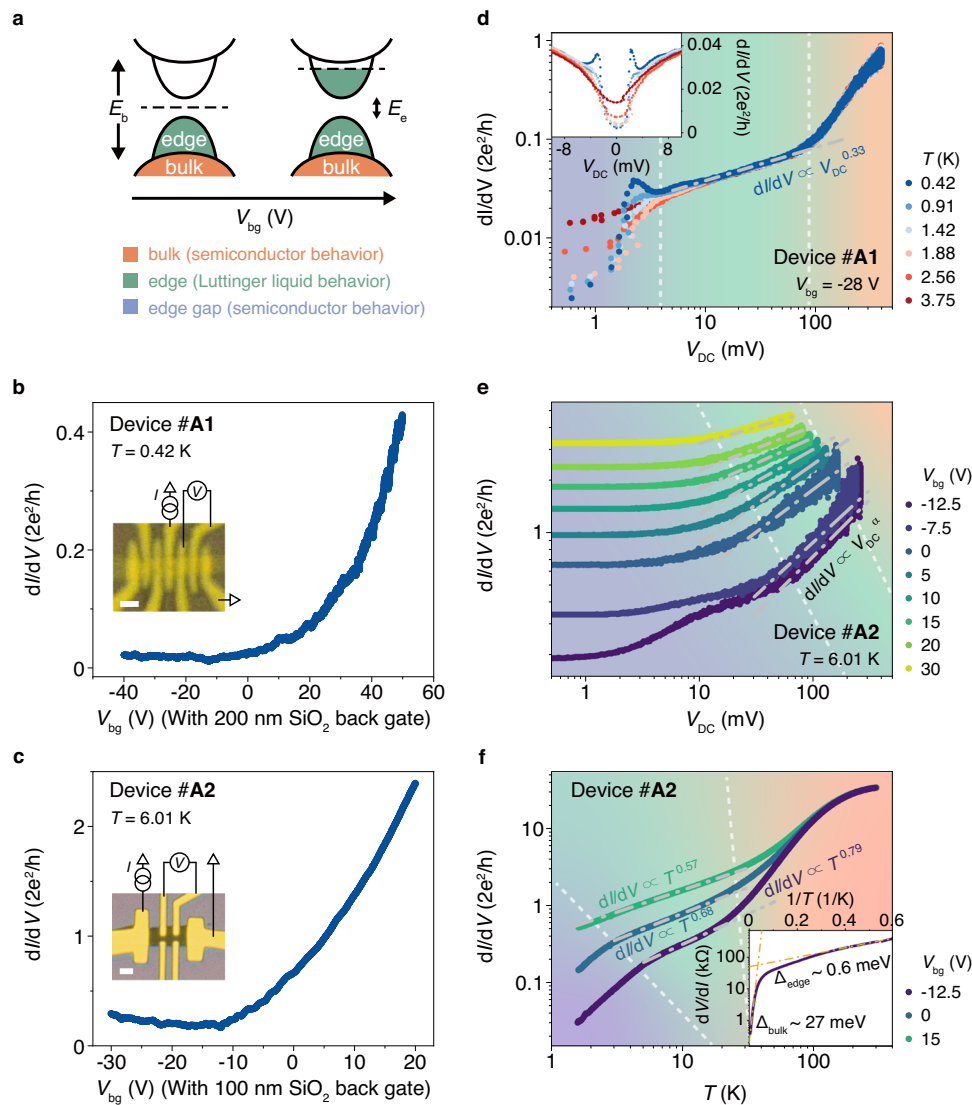


Fig. 2 | Electrical transport measurement for $\text{Ta}_2\text{Pd}_3\text{Te}_5$. **a** Sketch of Fermi level rising with V_{bg} . **b** dI/dV versus V_{bg} measured in device #A1 at $T = 0.42$ K. Inset: Optical image and schematic measurement configuration. Scale bar, 1 μm . **c** dI/dV versus V_{bg} measured in device #A2 at $T = 6.01$ K. Inset: Optical image and schematic measurement configuration. Scale bar, 2 μm . **d** Log-log plot of dI/dV versus V_{DC} measured in device #A1 at $V_{\text{bg}} = -28$ V and different T . Inset: The same data as main figure but plotted in linear scale and symmetric V_{DC} . **e** Log-log plot of dI/dV versus

V_{DC} measured in device #A2 at $T = 6.01$ K and different V_{bg} . **f** Log-log plot of temperature dependence dI/dV of device #A2 at different V_{bg} . Inset: $\log(dV/dI)$ v.s. $1/T$ plot of the temperature dependence resistance of device #A2 at $V_{\text{bg}} = -12.5$ V. The gray dot dash lines show the power-law behavior. The orange/green/purple region of the background shows the bulk semiconductor/edge Luttinger liquid/edge gap behavior.

conductance $(dI/dV)/T^{0.69}$ with exponent of -0.69 , which is extracted from $dI/dV(T)$ curve in Supplementary Fig. 2b, as y -axis and $eV_{\text{DC}}/k_{\text{B}}T$ (k_{B} is the Boltzmann constant) as x -axis. By this, all the curves converge together with a zero-energy anomaly, confirming the universal power-law correlation as well as LL behavior (similar behavior of device #A2 is shown in Supplementary Fig. 4 and more examples are in Supplementary Figs. 2, 3, and 12). We note that for $dI/dV(V_{\text{DC}})$ curves at the lowest temperature (e.g., $T < 12.9$ K in Fig. 4a), the low-bias regions exhibit edge gap behavior due to the 2D SOTI nature which limits the power-law and scaling ranges, so these low-temperature $dI/dV(V_{\text{DC}})$ curves should not obey the scaling behavior physically.

Furthermore, we linearly tune the power-law exponent α from -0.7 at CNP to below 0.1 at positive V_{bg} (Figs. 2e and 4c, here $\alpha = 0$ means FL). This reveals a tunability of the Coulomb interaction strength of 1D edge state, as well as the transition from LL of correlated 1D edge state to FL of extended high-dimensional bulk state along with

the rising of Fermi level. The exponent α is correlated with the strength of the Coulomb interaction and has been harnessed to test different types of interaction, e.g., Kondo effect in the helical edge state¹⁹, filling in the fractional quantum Hall¹⁷. The similar slope of tunability by gate voltage (also indicating the electron carrier density) in Fig. 4c from three devices might indicate a constant intrinsic interaction and provide a controllable approach to study the interaction strength and the quantum phase transition. Usually, one can use the exponent α to estimate the Luttinger liquid parameter K , which is an intrinsic parameter describing the electron-electron interactions in the system. But the numerical relationship between α and K intricately depends on the details of the system, such as the type/strength of tunnel barriers^{35–37}, edge state of fractional quantum Hall effect^{12, 38}/quantum spin Hall effect^{8, 19}, spin-orbit coupling³⁷, etc. The relation in our system is not clear yet, so we could not get the accurate calculation of K here and further theoretical modeling is needed.

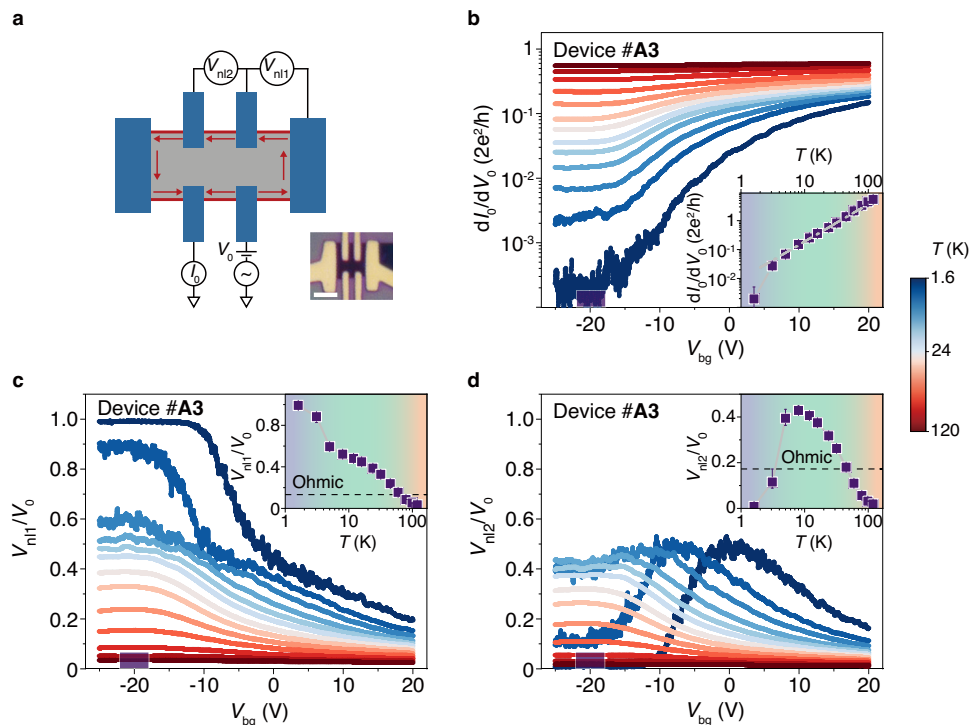


Fig. 3 | Nonlocal transport and edge states in $\text{Ta}_2\text{Pd}_3\text{Te}_5$. **a** Schematic nonlocal measurement configuration with Hall bar shape contacts (blue) on a $\text{Ta}_2\text{Pd}_3\text{Te}_5$ thin film (gray). The red lines are edges of the thin film and red arrows are current flow along edges. Inset: Optical image of device #A3. Scale bar, 2 μm . **b** Local differential conductance dI_0/dV_0 measured in device #A3 as a function of V_{bg} at differential T .

c, d Nonlocal voltage ratio V_{nll}/V_0 (**c**) and V_{nlz}/V_0 (**d**) versus V_{bg} at different T . Inset in (**b–d**): dI_0/dV_0 (**b**), V_{nll}/V_0 (**c**), and V_{nlz}/V_0 (**d**) versus T taken as the mean value at $V_{\text{bg}} = -22$ V to -18 V. The error bars show the full range of values spanned by the fluctuations. Dotted-lines are labels with simulation values of homogeneous 2D ohmic resistivity situation.

Robust and universal Luttinger liquid from micro- to macro-size

Here, we find there are two types of devices, among which we name the devices with distinguishable three regions as type A and the devices without E_e as type B. Because the edge conducting state is dominating at low energy, device B owns straight power-law traces with the absence of edge gap for both $dI/dV(T)$ and $dI/dV(V_{\text{DC}})$ curves, as well as large values of conductance, at small T and V_{DC} around CNP (Fig. 5a–c for device #B1 for example), similar to the curves at positive V_{bg} for device A (see the green curves in Fig. 2e, f). These power-law traces could also be scaled (Fig. 5c). Prominently, different sections of the same device could be scaled with the similar exponent (Supplementary Fig. 8). All these further confirm the intrinsic LL property of the edge conducting state, no matter w/o E_e . Interestingly, the exponent α from $dI/dV(T)$ curves is always larger than, sometimes nearly twice of, that from $dI/dV(V_{\text{DC}})$ curve (Figs. 2 and 5 and Supplementary Figs. 2–4 and 12–14), revealing both the inner LL–LL tunneling and FL–LL tunneling through electrodes are involved here^{35, 36, 39, 40}—the exponents of LL–LL junctions are twice of FL–LL junctions. So, the LL–LL tunneling becomes dominant and the exponent of $dI/dV(T)$ is $\alpha(\text{LL–LL})$ at low temperature due to the larger resistance of LL–LL junctions with larger exponents (with the assumption that both FL–LL and LL–LL junctions have similar resistance at room temperature). When we apply high bias, FL–LL junctions become dominant and the exponent of $dI/dV(V_{\text{DC}})$ is $\alpha(\text{FL–LL})$ (FL–LL junctions become more resistive because their resistance decreases more slowly)^{39, 40}.

This edge LL is of great stability and reproducibility, because it shows up in almost all the devices and maintains as long as at least one year. Remarkably, bulk samples with macroscopic geometry of ~ 100 μm , which we name as type C, also exhibit the nice LL behavior with a universal power-law correlation down to 100 mK (Fig. 5d–f and Supplementary Fig. 14). Interestingly, both of the thick devices and bulk

samples behave like type B without E_e . Thus, it gives us a hint that the reason for the absence of E_e might be the larger fluctuation of chemical potential or slight band variation due to the coupling of increasing layers. It is important to emphasize that there is no substantial difference between type A and B devices (and type C bulk samples); the only difference is the edge gap size between them. Type B devices and type C bulk samples do not exhibit distinct edge gap behavior down to the lowest temperature (~ 1.5 K for type B devices and ~ 0.1 K for type C samples) even at CNP in the measurement. But we do not deny the possibility that they will exhibit edge gap behavior at a lower temperature (see Supplementary Fig. 8g for device #B4_R as an example).

There is another point of interest, the kinks in the scaling curves of bulk samples with larger lead spacing are usually larger than that of thin films with smaller lead spacing (Fig. 5c, f as an example). In Luttinger liquid physics, the kink position in $eV/k_B T$ represents the number of the tunnel barriers in the 1D channel. We give a brief statistical result of this value for type B devices, type C bulk samples and Luttinger liquid region of type A devices in Supplementary Fig. 9a. It is clear that the number of tunnel barriers is positively correlated with the channel length.

Generally, Luttinger liquid behavior will be more credible if the power-law regions can extend to more than one decade. In our samples, at high temperature, thermal excitation will drive the sample exhibiting a bulk semiconducting behavior and at low temperature edge gap behavior will arise due to the 2D SOTI nature. The range of resistance change in power-law regions is smaller due to the small power exponents (usually < 1 for our devices/samples). Even so, the power-law range for almost all the type B devices/type C samples without edge gap and some of the type A devices can extend to more than one decade.

Apparent power-law dependence also shows up because of the environmental quantum fluctuation (EQF) or special region of variable

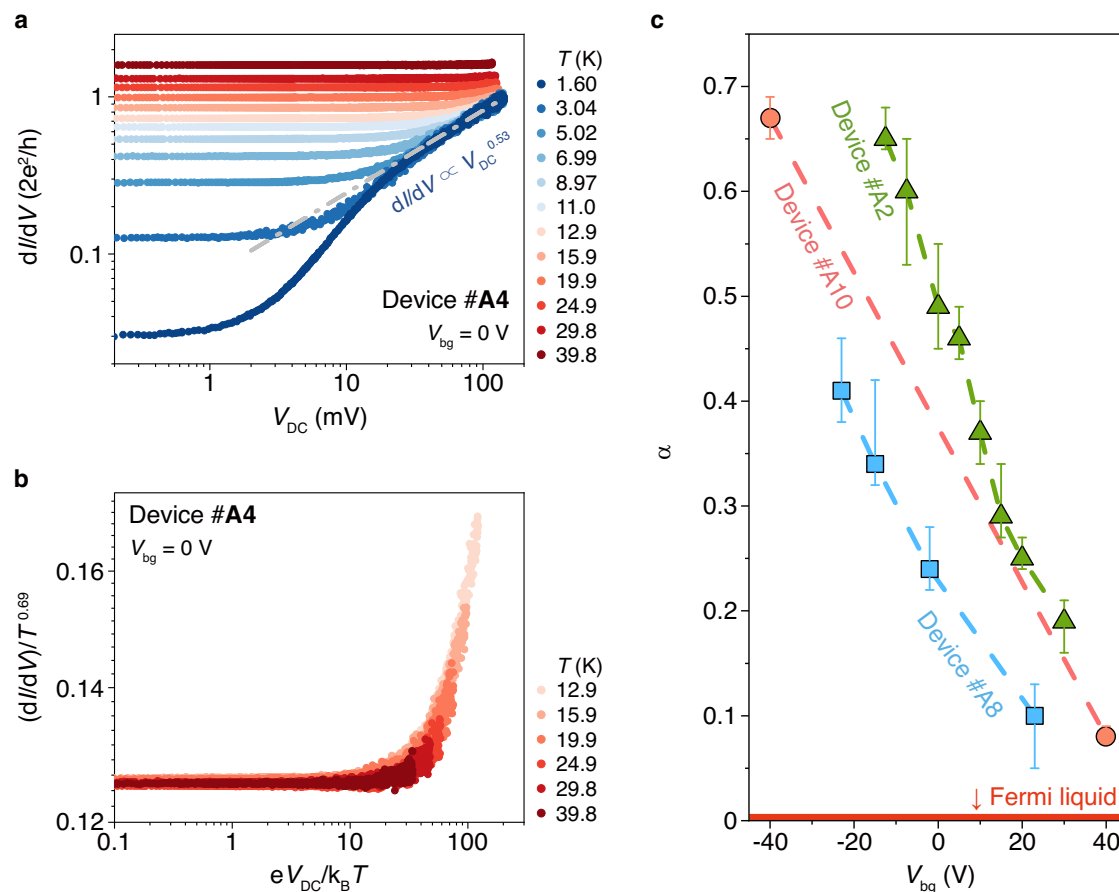


Fig. 4 | Tunable Luttinger liquid behaviors. **a** dI/dV versus V_{DC} measured in device #A4 at differential T with $V_{bg} = 0$ V. **b** The $dI/dV(V_{DC})$ curves without edge gap behavior in **(a)** (from $T = 12.9$ K to 39.8 K) are plotted as scaled conductance $(dI/dV)/T^{0.69}$ versus scaled temperature $eV_{DC}/k_B T$. All data collapses to a single curve indicating Luttinger liquid behaviors. $(dI/dV(V_{DC}))$ curves below $T = 12.9$ K exhibit edge

gap behavior due to the 2D SOTI nature, so they should not obey the scaling behavior physically. **c**, Gate tunable α in Luttinger liquid behaviors in dI/dV v.s. V_{DC} curves. The error bars reflect the uncertainty due to measurement noise (Raw data are included in Supplementary Fig. 12.).

range hopping (VRH)^{40,41–44}. For example, VRH from a disordered quasi-1D state due to inhomogeneity or folding lines in devices could show ‘apparent’ power-law behavior⁴⁴. We can exclude the above-mentioned reasons as follows. Firstly, the high quality of our devices with PMMA protecting layers (see “Devices fabrication” section in “Methods” for detail) can be verified by the optical images of the devices (inset of Figs. 2b, c and 3a, etc.). For a small number of devices with hBN as top capping layer (only 3 of the 22 devices—device #A6, Supplementary device #1 and #2), the optical images may exhibit contrast color (Supplementary Fig. 7) due to the unevenness of the top hBN on thick Ti/Au electrodes. These top capping layers are insulating and serve only as protecting layers, so they do not influence the transport behavior. This could also be confirmed by that we repeated robust power-law relation in various samples—with varying sizes from microscopic to macroscopic scale—at wide T and V_{DC} range other than specific samples with certain parameter range. Secondly, for VRH transport, the power exponent should become larger with increasing channel length⁴⁴. As a contrast, in our result, the power exponent is similar for microscopic devices and bulk samples with hundreds of micrometers (Supplementary Fig. 9b), inconsistent with VRH transport. Lastly, we have further proved the robust existence of clean edge states, instead of random 1D disordered channels by the sawtooth-shaped SQUID (superconducting quantum interference device) pattern in the Al-Ta₂Pd₃Te₅-Al Josephson junction⁴⁵.

The feature that semiconductor/Luttinger behavior at high/low T arising from bulk/edge will be more visual if we plot T -dependent

curves of several devices B and bulk samples C together in bulk conductivity σ (Fig. 5g) or edge sheet conductivity σ_{edge} (Fig. 5h). Because the values in high T region converge into the same order of magnitude in the former (orange region in Fig. 5g) while that in low T region in the latter (green region in Fig. 5h). As a contrast, the curves in top (bottom) surface sheet conductivity diverge in the entire T region (Supplementary Fig. 10), which excludes the possibility of the existence of top/bottom surface states. Moreover, the starting resistance for LL (R_{LL} , defined as 2% deviation of the extension resistance from power-law behavior in LL region) increases almost linearly with the number of squares in edge, \square_{edge} , for the devices with thickness of from ~ 4 nm to ~ 200 μ m over five orders of magnitude (Fig. 5i). This is the first experimental observation of the scale connection between atomic-LL (equals to ~ 6 layers) and macro-LL, and confirms the LL quantum state with correlation on the length scale and a universal feature independent of the microscopic details^{46,47}. It also supports the edge state calculated for the monolayer is generic for bulk sample due to the weak inter-layer coupling as the sketch in the inset of Fig. 5i shows. Such an in-gap 1D LL in the 2D sides of bulk Ta₂Pd₃Te₅ might boost a potential application of this giant anisotropic electrical transport, as well as the anisotropic heating transport.

The temperature-dependent electrical resistance of the bulk Ta₂Pd₃Te₅ has also been measured in previous works and the results are consistent with ours^{30,48}. Interestingly, as reported in ref. 48, the superconducting behavior can be observed in Ti- or W-doped

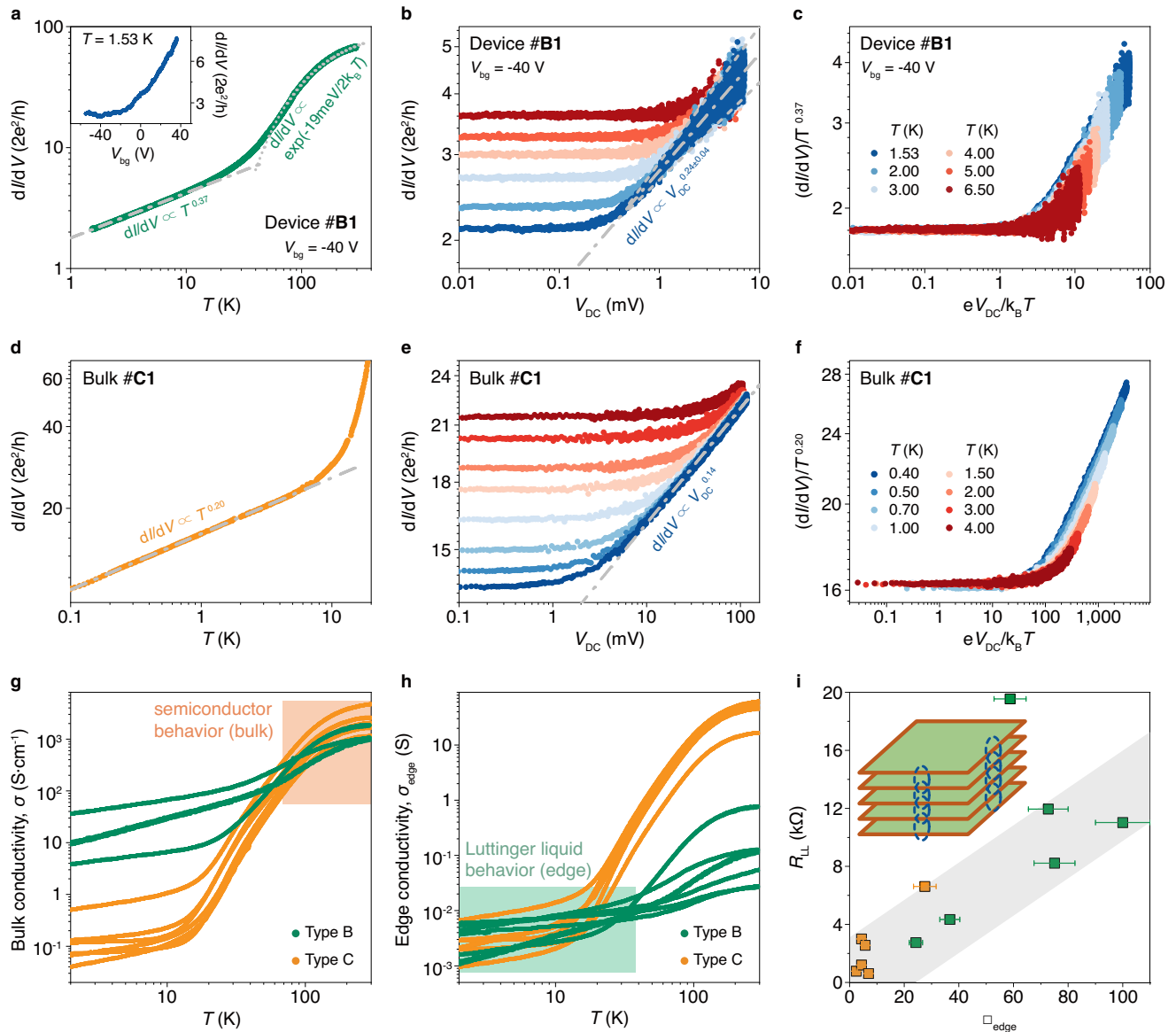


Fig. 5 | Universal Luttinger liquid behaviors from atomic to macroscopic scale.

a Temperature dependence dI/dV measured in device #B1 at $V_{bg} = -40$ V. The gray dot dash line and gray dot line show the power-law behavior and semiconductor behavior respectively. Inset: dI/dV versus V_{bg} at $T = 1.53$ K. **b** dI/dV versus V_{DC} measured in device #B1 at $V_{bg} = -40$ V and different T . Due to the noise in the large bias region of $dI/dV(V_{DC})$ curves, we use the median values to extract the exponent of power-law behavior (dot dash line) and use the upper and lower envelopes as fitting errors (dash lines)¹⁰. **c** The same data as (b), but plotted as scaled conductance $(dI/dV)/T^{0.37}$ versus scaled temperature $eV_{DC}/k_B T$. All data collapses to a single curve. **d** dI/dV versus T measured in bulk sample #C1. **e** dI/dV versus V_{DC} measured in bulk sample #C1 at different T . **f** The same data as (e), but plotted as

scaled conductance $(dI/dV)/T^{0.20}$ versus scaled temperature $eV_{DC}/k_B T$. **g**, **h** Temperature dependence of conductivity σ (**g**) and edge conductivity σ_{edge} (**h**, defined as conductance/thickness \times length) for type B (green line) and C (orange line) samples. Three devices measured with two-terminal configuration are not included in (**g**), others are four-terminal configuration. **i** Resistances of starting points of Luttinger liquid behaviors R_{LL} versus side surface square number \square_{edge} (defined as length/thickness) for type B and C samples, which follows an approximate linear dependence. The error bars reflect the uncertainty from length / thickness measurement. Uncertainties in y-axis are smaller than point size. Inset: Schematic of vdW stacking layers in $Ta_2Pd_3Te_5$. The red lines are edges of each layer and blue dotted lines are sketches of weak coupling between layers.

$Ta_2Pd_3Te_5$, indicating luxuriant physics phenomena hidden in $Ta_2Pd_3Te_5$ system.

Luttinger liquid phase diagram

We have mentioned the weak inter-layer coupling in Fig. 1d, but interestingly the bulk gap still varies with thickness. A plausible reason for the increasing bulk gap with decreasing thickness (summarized in Fig. 6a, calculated from the Arrhenius equation $\Delta = -2k_B(\partial \ln(dI/dV)/\partial T^{-1})$ by using the $dI/dV(T)$ curve) is that the insulating state is more robust in thinner devices due to the reduced screening effect to the Coulomb interaction. As the appearance of LL

relies on both of the bulk gap and edge gap, it is easy to perform a quantitative study of LL phase diagram. Figure 6b illustrates the summary of starting and ending temperature, T_1 and T_2 , of LL from $dI/dV(T)$ curves of devices with different thicknesses and results in a clear thickness-dependence phase diagram of bulk semiconducting FL, edge LL and edge gap. The temperature range of LL is adjustable over three orders of magnitude from -20 to 100 K in thin film devices to 0.1 – 7 K in bulk samples, exhibiting a large parameter space. We also find T_1 , which indicates the energy size of E_b , varies for a large temperature range with thickness but is still correlated with T_2 (indicating the size of E_e , Supplementary Fig. 11). This reveals that E_e

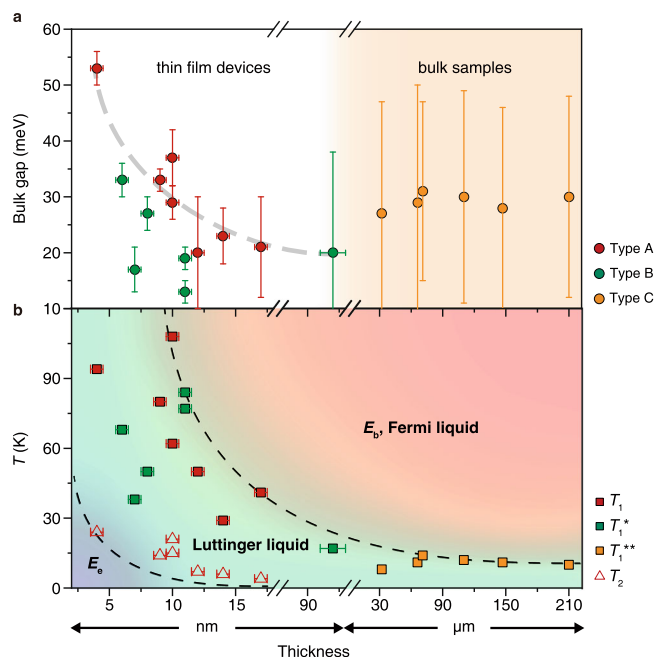


Fig. 6 | Luttinger liquid phase diagrams. **a** Thickness-dependent bulk gap extracted from $dI/dV(T)$ curves. The error bars in x -axis reflect the uncertainty from thickness measurement and error bars in y -axis show the ranges of bulk gap variation. **b** The Luttinger liquid phase transition temperature versus sample thickness. $T_1/T_1^+/T_1^{**}$: the transition temperatures from bulk Fermi-liquid semiconductor behaviors to edge Luttinger liquid behaviors for type A/B/C samples; T_2 : the transition temperatures from edge Luttinger liquid behaviors to edge gap behaviors for type A samples. The error bars reflect the uncertainty from thickness measurement. Uncertainties in y -axis are smaller than point size.

originates from the intrinsic band structure instead of other insulating state.

Summary

As such, this LL has not only extended the LL families to the more general boundary, beyond helical and chiral edges, of high-dimensional systems, but also remarkably promotes the reproducibility and enlarges parameter space including geometry, temperature (T) and chemical potential (μ). We conclude this LL possesses universality and robustness, as well as a full phase diagram with extensive range, complete data set and strong tunability. Therefore, this model system would have wide-reaching implications to understand quantum phases towards more complex systems, with a combination of strong correlation and topology, which is lack of useful and practical method to analyze before.

Methods

Density functional theory calculations

The first-principles calculations were performed within the framework of the density functional theory (DFT) using the projector augmented wave (PAW) method^{49, 50}, as implemented in Vienna ab-initio simulation package (VASP)^{51, 52}. PBE generalized gradient approximation exchange-correlations functional⁵³ was used. In the self-consistent process, $16 \times 4 \times 4$ k -point sampling grids were used, and the cut-off energy for plane wave expansion was 500 eV. The monolayer structure is extracted from the experimental bulk crystal, where inversion symmetry (IS) is slightly broken. With relaxation the symmetry of the relaxed monolayer becomes $Pmmn$ (No. 59). The PBE band structure shows that there is a small band overlap at Γ . The band representation analysis of the monolayer band structure shows that there is a remarkable double-band inversion on the Γ -Y line. In order to match

the experimental energy gap, we artificially upshift the conduction bands ($Ta-dz^2$ in the Wannier-based Hamiltonian) by 0.1 eV to remove the small band overlap.

Growth of $Ta_2Pd_3Te_5$ crystals

Single crystals of $Ta_2Pd_3Te_5$ were synthesized by self-flux method. Details can be found in ref. 29.

Devices fabrication

We have two kinds of fabrication for devices: one is coating devices with PMMA to prevent from surface oxidation and contamination, and using SiO_2/Si^+ as bottom gate (devices #A1-A5, #A7-A14, and #B1-B6); the other is using a graphite/hexagonal boron nitride (hBN) bottom gate and covering devices with hBN on top to protect devices (device #A6, Supplementary device #1 and #2).

For the first kind of devices: The $Ta_2Pd_3Te_5$ thin films were mechanically exfoliated onto SiO_2/Si^+ substrates and coated with PMMA in a glove box. The two-terminal/four-terminal/Hall bar devices were patterned using electron-beam lithography and moved into the glove box to develop. The Ti/Au electrodes were deposited using thermal evaporation instrument installed in the glove box. Then lifted-off the metal film and coated with PMMA once again without being moved out of the glove box. After these, we performed electron-beam lithography for the second time to pattern the Ti/Au pads in order that we could connect the pads and transport measurements sample holder using wire-bonding out of the glove box. The $Ta_2Pd_3Te_5$ thin films were in the nitrogen atmosphere glove box or coated with PMMA in the air during the whole fabrication process to prevent oxidation.

For the second kind of devices: We used polydimethylsiloxane (PDMS) to exfoliate graphite/hBN/ $Ta_2Pd_3Te_5$ flake and drop them on SiO_2/Si^+ substrates respectively on a micro-positioning stage in the glove box to build a graphite/hBN/ $Ta_2Pd_3Te_5$ stack. Then coat the substrate with PMMA without moving out of the glove box. The two-terminal/four-terminal/Hall bar devices were patterned using electron-beam lithography and moved into the glove box to develop. The Ti/Au electrodes were deposited using thermal evaporation instrument installed in the glove box. Then lifted-off the metal film and coated the device with hBN once again without being moved out of the glove box.

Electrical transport measurements

The electrical transport measurements were performed in cryostats (Oxford instruments dilution refrigerator with temperature range -10 mK–30 K, Oxford instruments ³He cryostats with temperature range -400 mK–30 K and Oxford instruments TeslatronPT with temperature range -1.5 K–300 K). The bottom gate voltage V_{bg} and d.c. bias were applied using Keithley 2400 or 2612. Standard lock-in measurements were taken with a frequency of 3–30 Hz with a small a.c. excitation below the thermal excitation range without specially marked. Note that due to the disorders and defects which could break the conducting channels in the edges of $Ta_2Pd_3Te_5$, the tunneling behaviors appear both in the electrodes–edge junctions (FL-LL) and edge–edge junctions (LL-LL)^{8, 36, 37}. So, we can observe the power law behavior of Luttinger liquid both in two-terminal and four-terminal/Hall bar configurations.

Note that due to the thickness of SiO_2 dielectric layers used to apply V_{bg} are different in device #A1 (200 nm) and #A2 (100 nm), the adjusting abilities are different. The thickness of SiO_2 is 100 nm if not specially marked in other devices.

Data availability

All data needed to evaluate the conclusions in the paper are present in the main text and/or the Supplementary Information. The authors declare that all of the raw data generated in this study have been deposited in Figshare (<https://doi.org/10.6084/m9.figshare.24407743>).

References

1. Tokura, Y. Quantum materials at the crossroads of strong correlation and topology. *Nat. Mater.* **21**, 971–973 (2022).
2. Zhou, Y., Kanoda, K. & Ng, T.-K. Quantum spin liquid states. *Rev. Mod. Phys.* **89**, 025003 (2017).
3. Raghu, S., Qi, X.-L., Honerkamp, C. & Zhang, S.-C. Topological Mott insulators. *Phys. Rev. Lett.* **100**, 156401 (2008).
4. Cao, Y. et al. Correlated insulator behaviour at half-filling in magic-angle graphene superlattices. *Nature* **556**, 80–84 (2018).
5. Xie, M. & MacDonald, A. H. Nature of the correlated insulator states in twisted bilayer graphene. *Phys. Rev. Lett.* **124**, 097601 (2020).
6. Hasan, M. Z. & Kane, C. L. Colloquium: Topological insulators. *Rev. Mod. Phys.* **82**, 23 (2010).
7. Qi, X.-L. & Zhang, S.-C. Topological insulators and superconductors. *Rev. Mod. Phys.* **83**, 54 (2011).
8. Li, T. et al. Observation of a helical Luttinger liquid in InAs/GaSb quantum spin Hall edges. *Phys. Rev. Lett.* **115**, 136804 (2015).
9. Strunz, J. et al. Interacting topological edge channels. *Nat. Phys.* **16**, 83–88 (2020).
10. Stühler, R. et al. Tomonaga–Luttinger liquid in the edge channels of a quantum spin Hall insulator. *Nat. Phys.* **16**, 47–51 (2020).
11. Milliken, F. P., Umbach, C. P. & Webb, R. A. Indications of a Luttinger liquid in the fractional quantum Hall regime. *Solid. State Commun.* **97**, 309–313 (1996).
12. Chang, A. M., Pfeiffer, L. N. & West, K. W. Observation of chiral Luttinger behavior in electron tunneling into fractional quantum Hall edges. *Phys. Rev. Lett.* **77**, 2538–2541 (1996).
13. Hilke, M., Tsui, D. C., Grayson, M., Pfeiffer, L. N. & West, K. W. Fermi liquid to Luttinger liquid transition at the edge of a two-dimensional electron gas. *Phys. Rev. Lett.* **87**, 186806 (2001).
14. Chang, A. M. Chiral Luttinger liquids at the fractional quantum Hall edge. *Rev. Mod. Phys.* **75**, 1449–1505 (2003).
15. Hashisaka, M., Hiyama, N., Akiho, T., Muraki, K. & Fujisawa, T. Waveform measurement of charge- and spin-density wavepackets in a chiral Tomonaga–Luttinger liquid. *Nat. Phys.* **13**, 559–562 (2017).
16. Randeria, M. T. et al. Interacting multi-channel topological boundary modes in a quantum Hall valley system. *Nature* **566**, 363–367 (2019).
17. Wen, X. G. Chiral Luttinger liquid and the edge excitations in the fractional quantum Hall states. *Phys. Rev. B* **41**, 12838–12844 (1990).
18. Kane, C. L. & Fisher, M. P. A. Transport in a one-channel Luttinger liquid. *Phys. Rev. Lett.* **68**, 1220–1223 (1992).
19. Maciejko, J. et al. Kondo effect in the helical edge liquid of the quantum spin Hall state. *Phys. Rev. Lett.* **102**, 256803 (2009).
20. Imambekov, A., Schmidt, T. L. & Glazman, L. I. One-dimensional quantum liquids: beyond the Luttinger liquid paradigm. *Rev. Mod. Phys.* **84**, 1253–1306 (2012).
21. Giamarchi, T. Some experimental tests of Tomonaga–Luttinger liquids. *Int. J. Mod. Phys. B* **26**, 1244004 (2012).
22. Xie, B. et al. Higher-order band topology. *Nat. Rev. Phys.* **3**, 520–532 (2021).
23. Ezawa, M. Higher-order topological insulators and semimetals on the breathing kagome and pyrochlore lattices. *Phys. Rev. Lett.* **120**, 026801 (2018).
24. Kunst, F. K., van Miert, G. & Bergholtz, E. J. Lattice models with exactly solvable topological hinge and corner states. *Phys. Rev. B* **97**, 241405 (2018).
25. Park, M. J., Kim, Y., Cho, G. Y. & Lee, S. Higher-order topological insulator in twisted bilayer graphene. *Phys. Rev. Lett.* **123**, 216803 (2019).
26. Sheng, X.-L. et al. Two-dimensional second-order topological insulator in graphdiyne. *Phys. Rev. Lett.* **123**, 256402 (2019).
27. Ren, Y., Qiao, Z. & Niu, Q. Engineering corner states from two-dimensional topological insulators. *Phys. Rev. Lett.* **124**, 166804 (2020).
28. Guo, Z., Deng, J., Xie, Y. & Wang, Z. Quadrupole topological insulators in $\text{Ta}_2\text{M}_3\text{Te}_5$ ($M=\text{Ni}$, Pd) monolayers. *npj Quantum Mater.* **7**, 1–6 (2022).
29. Guo, Z. et al. Quantum spin Hall effect in $\text{Ta}_2\text{M}_3\text{Te}_5$ ($M=\text{Pd}$, Ni). *Phys. Rev. B* **103**, 115145 (2021).
30. Wang, X. et al. Observation of topological edge states in the quantum spin Hall insulator $\text{Ta}_2\text{Pd}_3\text{Te}_5$. *Phys. Rev. B* **104**, L241408 (2021).
31. Gao, J. et al. Unconventional materials: the mismatch between electronic charge centers and atomic positions. *Sci. Bull.* **67**, 598–608 (2022).
32. Xu, Y. et al. Filling-enforced obstructed atomic insulators. Preprint at <https://arxiv.org/abs/2106.10276> (2021).
33. Fei, Z. et al. Edge conduction in monolayer WTe_2 . *Nat. Phys.* **13**, 677–682 (2017).
34. Aharon-Steinberg, A. et al. Long-range nontopological edge currents in charge-neutral graphene. *Nature* **593**, 528–534 (2021).
35. Bockrath, M. et al. Luttinger-liquid behaviour in carbon nanotubes. *Nature* **397**, 598–601 (1999).
36. Yao, Z., Postma, H. W. C., Balents, L. & Dekker, C. Carbon nanotube intramolecular junctions. *Nature* **402**, 273–276 (1999).
37. Hsu, C.-H. et al. Charge transport of a spin-orbit-coupled Luttinger liquid. *Phys. Rev. B* **100**, 195423 (2019).
38. Grayson, M., Tsui, D. C., Pfeiffer, L. N., West, K. W. & Chang, A. M. Continuum of chiral Luttinger liquids at the fractional quantum Hall edge. *Phys. Rev. Lett.* **80**, 1062–1065 (1998).
39. Venkataraman, L., Hong, Y. S. & Kim, P. Electron transport in a multichannel one-dimensional conductor: molybdenum selenide nanowires. *Phys. Rev. Lett.* **96**, 076601 (2006).
40. Wang, J. et al. A tied Fermi liquid to Luttinger liquid model for nonlinear transport in conducting polymers. *Nat. Commun.* **12**, 58 (2021).
41. Blumenstein, C. et al. Atomically controlled quantum chains hosting a Tomonaga–Luttinger liquid. *Nat. Phys.* **7**, 776–780 (2011).
42. Yi, W., Lu, L., Hu, H., Pan, Z. W. & Xie, S. S. Tunneling into multi-walled carbon nanotubes: Coulomb blockade and the Fano resonance. *Phys. Rev. Lett.* **91**, 076801 (2003).
43. Fogler, M. M., Malinin, S. V. & Nattermann, T. Coulomb blockade and transport in a chain of one-dimensional quantum dots. *Phys. Rev. Lett.* **97**, 096601 (2006).
44. Rodin, A. S. & Fogler, M. M. Apparent power-law behavior of conductance in disordered quasi-one-dimensional systems. *Phys. Rev. Lett.* **105**, 106801 (2010).
45. Li, Y. P. et al. Interfering Josephson diode effect and magnetochiral anisotropy in $\text{Ta}_2\text{Pd}_3\text{Te}_5$ asymmetric edge interferometer. Preprint at <https://arxiv.org/abs/2306.08478> (2023).
46. Zaliznyak, I. A. A glimpse of a Luttinger liquid. *Nat. Mater.* **4**, 273–275 (2005).
47. Lake, B., Tennant, D. A., Frost, C. D. & Nagler, S. E. Quantum criticality and universal scaling of a quantum antiferromagnet. *Nat. Mater.* **4**, 329–334 (2005).
48. Higashihara, N. et al. Superconductivity in $\text{Nb}_2\text{Pd}_3\text{Te}_5$ and Chemically-doped $\text{Ta}_2\text{Pd}_3\text{Te}_5$. *J. Phys. Soc. Jpn.* **90**, 063705 (2021).
49. Blöchl, P. E. Projector augmented-wave method. *Phys. Rev. B* **50**, 17953–17979 (1994).
50. Kresse, G. & Joubert, D. From ultrasoft pseudopotentials to the projector augmented-wave method. *Phys. Rev. B* **59**, 1758–1775 (1999).
51. Kresse, G. & Furthmüller, J. Efficiency of ab-initio total energy calculations for metals and semiconductors using a plane-wave basis set. *Comput. Mater. Sci.* **6**, 15–50 (1996).
52. Kresse, G. & Furthmüller, J. Efficient iterative schemes for ab initio total-energy calculations using a plane-wave basis set. *Phys. Rev. B* **54**, 11169–11186 (1996).
53. Perdew, J. P., Burke, K. & Ernzerhof, M. Generalized gradient approximation made simple. *Phys. Rev. Lett.* **77**, 3865–3868 (1996).

Acknowledgements

We are grateful to T. Xiang, J.P. Hu, Y. Zhou, Y. Wan, M. Cheng, B.J. Feng, and Z.Y. Sun for discussions. The work of J.S., L.L., F.Q. and G.L. were supported by the Beijing Natural Science Foundation (Grant No. JQ23022), the Strategic Priority Research Program B of Chinese Academy of Sciences (Grant No. XDB33000000), the Beijing Nova Program (Grant No. Z211100002121144), the National Natural Science Foundation of China (Grant Nos. 92065203 and 12174430), and the Synergetic Extreme Condition User Facility (SECUF). The work of other authors were supported by the National Natural Science Foundation of China (Grant Nos. 11974395, 12188101, U2032204, U1832202, U22A6005, 62022089, 11888101, 52072400 and 52025025), the Strategic Priority Research Program of the Chinese Academy of Sciences (Grant Nos. XDB33000000, XDB33030000 and XDB28000000), the National Key Research and Development Program of China (Grant Nos. 2022YFA1403800, 2021YFA1401800 and 2019YFA0308000), the Informatization Plan of Chinese Academy of Sciences (Grant No. CAS-WX2021SF-0102), the Chongqing Outstanding Youth Fund (Grant No. 2021ZX0400005), the China Postdoctoral Science Foundation (Grant Nos. 2021M703462, 2021TQ0356 and 2021M703461), the “Dreamline” beamline of Shanghai Synchrotron Radiation Facility (SSRF), the Center for Materials Genome, and the Synergetic Extreme Condition User Facility (SECUF).

Author contributions

J.S. conceived and designed the experiment. A.W., Y.L., G.Y., Q.Z., D.Q., H.W. and X.G. fabricated devices and performed the transport measurements, supervised by G.L, F.Q. L.L., and J.S. D.Y. and Y.S. grew bulk $Ta_2Pd_3Te_5$ crystals. F.M., Q.Z. and L.G. performed the STEM measurements. J.H. and T.Q. performed the ARPES measurements. Z.G., J.G., and Z.W. performed the theoretical modeling. H.Y. and X.Z. provided some supports on thin film exfoliation and devices fabrication. A.W., Y.L., G.Y. and J.S. analyzed the data and wrote the manuscript, with input from all authors.

Competing interests

The authors declare no competing interests.

Additional information

Supplementary information The online version contains supplementary material available at <https://doi.org/10.1038/s41467-023-43361-5>.

Correspondence and requests for materials should be addressed to Youguo Shi, Zhijun Wang, Li Lu or Jie Shen.

Peer review information *Nature Communications* thanks the anonymous reviewers for their contribution to the peer review of this work.

Reprints and permissions information is available at <http://www.nature.com/reprints>

Publisher’s note Springer Nature remains neutral with regard to jurisdictional claims in published maps and institutional affiliations.

Open Access This article is licensed under a Creative Commons Attribution 4.0 International License, which permits use, sharing, adaptation, distribution and reproduction in any medium or format, as long as you give appropriate credit to the original author(s) and the source, provide a link to the Creative Commons license, and indicate if changes were made. The images or other third party material in this article are included in the article’s Creative Commons license, unless indicated otherwise in a credit line to the material. If material is not included in the article’s Creative Commons license and your intended use is not permitted by statutory regulation or exceeds the permitted use, you will need to obtain permission directly from the copyright holder. To view a copy of this license, visit <http://creativecommons.org/licenses/by/4.0/>.

© The Author(s) 2023